# Estimating the 4DVAR analysis error of GODAE products

**Brian S. Powell · Andrew M. Moore**

**Abstract** We explore the ocean circulation estimates obtained by assimilating observational products made available by the Global Ocean Data Assimilation Experiment (GODAE) and other sources in an incremental, four-dimensional variational data assimilation system for the Intra-Americas Sea. Estimates of the analysis error (formally, the inverse Hessian matrix) are computed during the assimilation procedure. Comparing the impact of differing sea surface height and sea surface temperature products on both the final analysis error and difference between the model state estimates, we find that assimilating GODAE and non-GODAE products yields differences between the model and observations that are comparable to the differences between the observation products themselves. While the resulting analysis error estimates depend on the configuration of the assimilation system, the basic spatial structures of the standard deviations of the ocean circulation estimates are fairly robust and reveal that the assimilation procedure is capable of reducing the circulation uncertainty when only surface data are assimilated.

**Keywords** 4DVAR · Hessian · Analysis error · Data assimilation · GODAE

B. S. Powell (✉)
Department of Oceanography, University of Hawai'i
at Mānoa, Honolulu, HI, 96822 USA
e-mail: powellb@hawaii.edu

B. S. Powell · A. M. Moore
Department of Ocean Sciences, University of California,
Santa Cruz, CA, 95064 USA

## 1 Introduction

The Global Ocean Data Assimilation Experiment (GODAE) is aimed at replicating the success of numerical weather prediction in the ocean community by turning monitoring, analysis, and prediction into standard activities. An important component of the experiment is the creation and distribution of quality-controlled observational ocean products, and how these products compare to other available sources of data is of considerable interest. In this paper, we use a four-dimensional variational (4DVAR) data assimilation system with both GODAE and non-GODAE observational products and compare the differences between the resulting estimates of the ocean circulation. Data assimilation is the procedure for combining a model with observational data to yield an estimate of the ocean circulation that is more reliable than either alone. By using the various observational products within the assimilation system, we attempt to highlight and understand the differences between various commonly used observational products.

A near-real-time (NRT) ocean assimilation and ensemble prediction system was developed for the Intra-Americas Sea (IAS) by Powell et al. ([2008]), and the system was run onboard the Royal Caribbean Cruise Line's *Explorer of the Seas* for the majority of 2007, generating weekly assimilation and forecast estimates of the IAS. Part of the experiment was to test the efficacy of ship-board predictive capabilities. Two NRT satellite products were used along with the in situ acoustic doppler current profiler (ADCP) measurements collected by instruments mounted to the ship. Because of the realtime constraints and limited computing resources on the ship, the resolution of the

model was relatively coarse; however, the NRT system serves as an excellent testbed for calculating the analysis error from the available observational products. For this study, we compare the results of assimilating NRT data from the period January–August, 2007, with similar experiments in which nonrealtime, research-quality data products were used.

Access to NRT observational data is often restricted [particularly the sea surface height (SSH) from Geosat Follow-On (GFO), Envisat, etc.], and the processing of NRT data is a nontrivial undertaking (e.g., cloud removal). Therefore, we must rely on processed data products that may combine a number of instruments, usually as mapped products that are typically created via an optimal interpolation scheme (e.g., Leben et al. 2002). Such products may not be ideally suited for data assimilation (particularly 4DVAR, which allows for asynoptic observations). However, in delayed time, mapped products can be a valuable source of quality-controlled observational information.

The goal of this paper is to compare the relative uncertainties that result in ocean circulation estimates for the IAS that are obtained by assimilating both GODAE and non-GODAE mapped products into a model. Our intention is to highlight the differences that result when using different observational products and how each may contribute to the uncertainty of the resulting circulation estimates. In Section 2, we introduce the model and present the mathematical background for determining the assimilation analysis error that is used as a measure of the uncertainty in the resulting ocean circulation estimates. In Section 3, we describe the sources of data and illustrate the differences between the observed data products. The results of assimilating each data product are presented in Section 4, and the comparisons of the estimated final analysis error are described in Section 5, followed by a summary and conclusions in Section 6.

## 2 Description

We use the Regional Ocean Modeling System (ROMS): a free-surface, hydrostatic, primitive equation model discretized with a terrain-following vertical coordinate system (Shchepetkin and McWilliams 2005). The model has multiple subgridscale parameterizations of vertical mixing along with several options for open boundary conditions. In the present study, ROMS has been configured for the IAS region at 1/3° horizontal resolution with 30 terrain-following vertical levels. The relatively coarse horizontal resolution was a necessary compromise between the computational expense of the data

assimilation procedure and operation of the assimilation system in realtime. The model uses third-order horizontal advection with the generic length scale vertical mixing scheme (Warner et al. 2005) and $k$-$kl$ mixing coefficients corresponding to Mellor–Yamada level 2.5.

There are two open boundaries in the IAS domain; the northern boundary, which spans part of the North Atlantic, and the eastern boundary, which includes the equatorial Atlantic and northeast Brazilian Current retroflection. The model boundary conditions were configured to conserve volume via a Chapman condition on the free surface and a Flather condition for the 2D momentum, and clamped to the 3D momentum and tracers (Marchesiello et al. 2001). The data for the clamped boundary conditions were derived from a long North Atlantic ROMS simulation run at 1/6° with National Centers for Environmental Prediction (NCEP) forcing (Haidvogel et al. 2000). Using a 6-year time series of the North Atlantic simulation from 1990 to 1996, monthly climatological open boundary conditions were computed for the IAS model. Climatological boundaries were used because the North Atlantic ROMS simulation does not coincide with the assimilation period and because boundary data are not available during the forecast periods.

Atmospheric forcing was derived from the NCEP/NCAR reanalysis product (Kistler et al. 2001) at 2° spatial resolution every 6 h. The ocean surface heat flux was computed via the COARE algorithm (Fairall et al. 1996) using standard 2- and 10-m forcings from the NCEP/NCAR reanalysis. To allow for known uncertainties in the net surface freshwater flux and the lack of fresh water discharge data from major rivers in the region, the model surface salinity was relaxed to the monthly Levitus climatology (Levitus et al. 1994) with a relaxation time of 50 days.

The data assimilation scheme used is the incremental strong constraint four-dimensional variational data assimilation (IS4DVAR) originally developed by Courtier et al. (1994) for operational numerical weather prediction. One advantage of IS4DVAR is that asynoptic observations can be continuously assimilated into the model over a long assimilation window using the ocean dynamics as a dynamical constraint on the resulting circulation estimate. For the current experiments, a 14-day assimilation window provides a balance between the validity of certain linear assumptions that are inherent in IS4DVAR and the amount of data that is available to constrain the model solution. Our main focus is the analysis error of the assimilated circulation estimate. A complete description of the ROMS implementation of IS4DVAR can be found in Powell et al. (2008).

In IS4DVAR, the model initial conditions, $\Psi_b(0)$, are adjusted to create a time-dependent circulation, $\Psi(t)$, that—in a least-squares sense—minimizes the difference, $\mathbf{d}_i$, between the model and observations, $\mathbf{y_i}$ at $t_i$, where $\mathbf{d}_i = \mathbf{y}_i - \mathbf{H}_i\Psi_b(t_i)$ is referred to as the innovation vector; $\Psi_b(t)$ is the background circulation from the initial condition, $\Psi_b(0)$, through the nonlinear model; and $\mathbf{H}_i$ is an operator that maps model gridpoint values to the observation points. We seek the initial condition, $\Psi(0) = \Psi_b(0) + \delta\psi$, that minimizes the quadratic cost function,

$$
J(\delta\psi) = \frac{1}{2}\delta\psi^T\mathbf{B}^{-1}\delta\psi
$$
$$
+ \frac{1}{2}\sum_{i=1}^{N}(\mathbf{G}_i\delta\psi - \mathbf{d}_i)^T\mathbf{O}^{-1}(\mathbf{G}_i\delta\psi - \mathbf{d}_i), \quad (1)
$$

where $N$ is the number of observations, $\delta\psi$ are perturbations to $\Psi_b(0)$, $\mathbf{B}$ is the background error covariance matrix, $\mathbf{O}$ is the covariance matrix of observation errors and error of representativeness, and $\mathbf{G}_i = \mathbf{H}_i\mathbf{M}$ where $\mathbf{M}$ represents the integration of the tangent-linear model linearized about $\Psi(t)$.

The background error covariance matrix, $\mathbf{B}$, acts as an additional constraint and regularization of the model solution, and penalizes deviations of $\Psi(0)$ from the background, $\Psi_b(0)$. Because of the size of the current problem ($O(10^7) \times O(10^7)$), $\mathbf{B}$ cannot be computed directly or stored but, instead, is estimated and modeled as the solution of a diffusion equation (Derber and Rosati 1989; Weaver and Courtier 2001). In summary, $\mathbf{B}$ is factorized as

$$
\mathbf{B} = \mathbf{K}_b\,\mathbf{\Sigma}\,\mathbf{\Lambda}\mathbf{L}_v^{\frac{1}{2}}\mathbf{L}_h\mathbf{L}_v^{\frac{1}{2}}\mathbf{\Sigma}\,\mathbf{\Lambda}\mathbf{K}_b^T, \quad (2)
$$

where $\mathbf{K}_b$ are multivariate covariance operators; $\mathbf{\Sigma}$ is a diagonal matrix of the background error standard deviations; and $\mathbf{\Lambda}$, $\mathbf{L}_v$, and $\mathbf{L}_h$ model the Gaussian correlation functions. $\mathbf{L}_v$ and $\mathbf{L}_h$ represent the vertical and horizontal correlation functions of the unbalanced univariate errors in $\Psi_b(0)$ and, in the current implementation, are assumed to be isotropic and homogenous and modeled as solutions of a diffusion equation following Weaver and Courtier (2001). For our application, the vertical and horizontal correlation lengths are 100 m and 80 km, respectively. $\mathbf{\Lambda}$ is a diagonal matrix of normalization coefficients required to ensure that the correlation functions are bounded by $\pm 1$. The $\mathbf{\Sigma}$ matrices were calculated from a 16-year (1990–2006) forward model run (without data assimilation) under the assumption that errors in $\Psi_b(0)$ can—at least initially—be represented as the differences between randomly chosen ocean states and are given by the model

climatological variance. The $\mathbf{K}_b$ term provides multivariate covariance information (such as geostrophy); however, in the current implementation, $\mathbf{K}_b$ is replaced by the identity matrix, in which case, $\mathbf{B}$ is a block-diagonal, univariate matrix. This does not imply that the multivariate nature of the ocean dynamics is ignored since the tangent linear model (inherent in $\mathbf{G}$) couples the various components of the perturbations via the model dynamics; however, currently, only univariate statistical coupling in $\mathbf{B}$ is used to provide constraint to the cost function Eq. 1.

The observation error and error of representativeness are combined in the diagonal matrix, $\mathbf{O}$, coupling both the instrument error and the uncertainty in the ability of the model to represent those aspects of the circulation captured by the observations but unresolved by the model. For each observational product used, the observations were averaged into bins corresponding to the model grid cells and assimilated as "super" observations. This has three advantages. First, the variance of the observations relative to the super observation in each grid cell provides an estimate of the error of representativeness. This variance is used for the diagonal elements of $\mathbf{O}$ unless it is smaller than the instrument error described in Section 3. Second, spatial averaging helps remove small-scale features captured by the observations that are unresolved by the model. Lastly, using the available observations to estimate the error of representativeness gives a spatially and temporally varying error variance as well as objective, independent estimates of $\mathbf{O}$ for each product used.

At the minimum of Eq. 1, the cost function gradient, $\partial J/\partial\delta\psi$, vanishes and:

$$
\delta\psi_a \equiv \delta\psi = \left(\mathbf{B}^{-1} + \sum_{i=1}^{N}\mathbf{G}_i^T\mathbf{O}^{-1}\mathbf{G}_i\right)^{-1}\sum_{i=1}^{N}\mathbf{G}_i^T\mathbf{O}^{-1}\mathbf{d}_i,
$$
$$
(3)
$$

where $\delta\psi_a$ is referred to as the analysis increment, which is the desired least-squares solution of the data assimilation procedure, and $\mathbf{G}_i^T = \mathbf{M}^T\mathbf{H}_i^T$, where $\mathbf{M}^T$ represents the integration of the adjoint model linearized about $\Psi(t)$. Because of the large dimension of the problem, $\delta\psi_a$ cannot be computed directly, but is identified iteratively using a conjugate-gradient method (Fisher 1998; Tshimanga et al. 2008) via the Lanczos algorithm (Golub and Van Loan 1989; Fisher and Courtier 1995). A sequence of linear least-squares estimates of $\delta\psi_a$ are computed within the so-called "inner-loops" with periodic recalculation of $\Psi(t)$ during so-called "outer-loops," about which the linear model, $\mathbf{M}$, is linearized during each inner-loop. For these

experiments, we used a single outer-loop with 30 inner-loops to estimate $\delta\psi_a$.

Because $\mathbf{O}$ has far smaller dimension than $\mathbf{B}$, the properties of $J$ (and $\partial J/\partial\delta\psi$) are dominated by $\mathbf{B}$. In the ROMS implementation of IS4DVAR, $J$ is minimized by first performing a change of variable, $\mathbf{v} = \mathbf{B}^{-\frac{1}{2}}\delta\psi$, that we will refer to as *v-space*. The resulting $J$ cast into *v-space* is better conditioned for minimization by the conjugate-gradient method and is given by

$$J_v(\mathbf{v}) = \frac{1}{2}\mathbf{v}^T\mathbf{v} + \frac{1}{2}\sum_{i=1}^{N}\left(\mathbf{G}_i\mathbf{B}^{\frac{1}{2}}\mathbf{v} - \mathbf{d}_i\right)^T\mathbf{O}^{-1}\left(\mathbf{G}_i\mathbf{B}^{\frac{1}{2}}\mathbf{v} - \mathbf{d}_i\right).$$

(4)

We wish to estimate the analysis error, denoted $\mathbf{E}_a$, of the assimilated model ocean state estimate, $\Psi_b(0) + \delta\psi_a$ to elucidate how the prior uncertainties in $\Psi_b(0)$ (represented by $\mathbf{B}$) are reduced by assimilating the various observational products. For IS4DVAR, $\mathbf{E}_a$ is given by the inverse of the Hessian matrix of the cost function (Draper and Smith 1966). In *v-space*, the Hessian is given by:

$$\mathcal{H}_v = \frac{\partial^2 J_v}{\partial\delta\psi^2} = \mathbf{I} + \mathbf{B}^{\frac{T}{2}}\left(\sum_{i=1}^{N}\mathbf{G}_i^T\mathbf{O}^{-1}\mathbf{G}_i\right)\mathbf{B}^{\frac{1}{2}}.$$

(5)

Fisher and Courtier (1995) present three methods of obtaining an estimate of the inverse Hessian: randomization; via a subset of Hessian eigenvectors with an application in observational space shown by Gelaro et al. (2002); and, the Broyden–Fletcher–Goldfarb–Shanno method with a recent example by Gejadze et al. (2008). As discussed, we use a Lanczos algorithm for the conjugate gradient method, and during each iteration of the minimization procedure, the leading eigenvectors of $\mathcal{H}_v$ can be estimated to a specified accuracy. By Fisher and Courtier (1995), a reduced rank approximation of $\mathcal{H}_v$ can be computed from a subset of the Hessian eigenvectors, $\mathbf{e}^v$, by

$$\mathcal{H}_v \approx \mathbf{I} + \sum_{i=1}^{k}(\lambda_i - 1)\,\mathbf{e}_i^v\left(\mathbf{e}_i^v\right)^T,$$

(6)

where $k$ is the number of computed eigenvectors of $\mathcal{H}_v$, $\lambda_i$ are the corresponding eigenvalues (unchanged by the transformation to *v-space*), and $k \ll \text{rank}(\mathcal{H}_v)$. According to Eq. 6, many of the eigenvalues of $\mathcal{H}_v$ will be clustered about a value of 1, which is also the smallest value that any eigenvalue of $\mathcal{H}_v$ can have (Fisher and Courtier 1995). Following the procedure used at the European Centre for Medium-Range Weather Forecasts (http://www.ecmwf.int/research/ifsdocs/CY31r1),

the inverse of $\mathcal{H}_v$ can be used to calculate an estimate of $\mathbf{E}_a$.

First, Eq. 6 is written in the form $\mathcal{H}_v \approx \mathbf{I} + \mathbf{S}\mathbf{I}\mathbf{S}^T$, where $\mathbf{S} = (\mathbf{s}_i)$ and $\mathbf{s}_i = (\lambda_i - 1)^{\frac{1}{2}}\,\mathbf{e}_i^v$. The inverse of $\mathcal{H}_v$ is computed using the Sherman–Morrison–Woodbury matrix identity (Golub and Van Loan 1989), which yields: $\mathcal{H}_v^{-1} = \mathbf{I} - \mathbf{S}\left(\mathbf{I}_k + \mathbf{S}^T\mathbf{S}\right)^{-1}\mathbf{S}^T$, where $\mathbf{I}_k$ is the $(k \times k)$ identity matrix.

During IS4DVAR, we identify the leading $k$ eigenvectors of $\mathcal{H}_v$ for each assimilation cycle; however, to fully estimate the analysis error, we require the leading eigenvectors of $\mathcal{H}_v^{-1}$, which correspond to the trailing eigenvectors of $\mathcal{H}_v$. This poses a dilemma because our estimate of $\mathbf{E}_a$ is the least significant portion of the eigenspectrum. We are currently working on a modification to the IS4DVAR algorithm to identify eigenvectors from both ends of the eigenspectrum of $\mathcal{H}_v$, but for now, we explore what information can be derived from the leading eigenvectors of $\mathcal{H}_v$. In Section 5, we compare different estimates of $\mathbf{E}_a$ for the same assimilation experiments.

For each analysis, the estimate of $\mathcal{H}_v^{-1}$ must be transformed back into physical space. From the definition of *v-space*,

$$\mathbf{E}_a = \mathbf{B}^{\frac{T}{2}}\mathcal{H}_v^{-1}\mathbf{B}^{\frac{1}{2}} = \mathbf{B} - \mathbf{B}^{\frac{T}{2}}\mathbf{S}\left(\mathbf{I}_k + \mathbf{S}^T\mathbf{S}\right)^{-1}\mathbf{S}^T\mathbf{B}^{\frac{1}{2}}.$$

(7)

From Eqs. 7 and 5, it is apparent that $\mathbf{E}_a$ depends only on $\mathbf{B}$, $\mathbf{O}$, and integrations of the adjoint ($\mathbf{M}^T$) and tangent-linear ($\mathbf{M}$) models, which create the covariance of the circulation scaled by the observation error; therefore, $\mathbf{E}_a$ is independent of the observational values. Neither $\mathbf{B}$ nor $\mathbf{S}$ can be computed and stored due to their large dimension, so we will limit our analysis to the diagonal elements of $\mathbf{E}_a$, which represent the univariate component of the analysis error variance.

It should be expected that, for most observation locations, the corresponding variance in $\mathbf{B}$ will be larger than $\mathbf{O}$; otherwise, the model grid value is considered more reliable than the observation in Eq. 1. The diagonal of $\mathbf{O}$ and univariate terms of $\mathbf{B}$ are specified a priori as described above. Comparing the diagonal of $\mathbf{B}$ at observation points with the appropriate diagonal elements of $\mathbf{O}$ for each observational product, we find that—on average—the observation errors are less than 10% of the corresponding background error. There are regions in the North Atlantic where the background error is less than the observation error; whereas, in the GOM, the background errors are much larger than the observation errors. We find that, in the Caribbean, the variance of the observation error in sea surface temperature (SST) are $\sim$ 30% of the background SST

error variance. A consequence of large uncertainty in **B** is that the Hessian eigenvectors will have maximum amplitude in the regions where the background error is largest. Ideally, **B** should be updated after several assimilation cycles as per Parrish and Derber (1992); however, for the experiments presented here, **B** was not updated.

## 3 Data analysis

From November 2006 through July 2007, four independently produced datasets were compared: two SSH products and two SST products. All products originate from similar satellite measurements; however, the choice of satellites, optimal interpolation method, data flagging, and processing procedures are independent for each product. As noted earlier, each of the products used employs a temporal and spatial optimal interpolation scheme to combine measurements from several data sources.

### 3.1 Sea surface height data

For the SSH measurements, we used the GODAE merged altimeter SSH anomaly produced by Ssalto/Duacs and distributed by Aviso, with support from *Centre national d'études spatiales* (CNES). These anomalies are relative to the CNES dynamic SSH mean, but the geoid and steric signals remain. The spatial resolution of the data are 0.3°, and are available as daily composites. The publicly available product lags the current day by approximately 1 month. The merged product uses all available altimetry data (Jason-1, Envisat, and GFO) during the time period. Pascual et al. (2007) found that, with two satellites, the average error was just over 2.2 cm root mean square (RMS); however, the actual error value was found to be larger than the mapping error alone (Le Traon et al. 2001). In the assignment of **O**, the minimum observational error of representativeness for the Aviso SSH was chosen to be 4 cm.

The second dynamic height product is the NRT SSH anomaly data available from the Colorado Center for Astrodynamics (CCAR) at the University of Colorado (Leben et al. 2002). The merged data from the realtime altimeter streams are created at 0.25° on a daily basis, providing maps of daily observed SSH anomalies. This merged product uses the Jason-1, Envisat, and GFO satellites with a different optimal interpolation scheme than the Aviso product. For consistency, the same minimum error of representativeness was used in

the assimilation of the CCAR SSH (4 cm) as with the Aviso SSH. The NRT CCAR SSH is a capable first-look product, but it is limited in accuracy by a lack of posterior data in the temporal interpolation and quality-controlled observations compared to time-delayed validated science data. This has the potential of introducing additional errors and uncertainties.

Beginning in November 2006, the Jason-1 real-time orbital information was degraded due to the diminished tracking ability of the onboard GPS receiver (S. Desai, personal communication). Accurate orbital height corrections are made during postprocessing, but this information is not available in NRT for the CCAR product. Corrections can be made by using the additional satellite information from GFO and Envisat. Compounding this issue, GFO was offline from January 2007 into April 2007 due to power problems. These issues combine to seriously degrade the quality of the CCAR SSH product during the first half of this experiment.

In order to assimilate the SSH into ROMS, the anomalies must be converted into a total dynamic height consistent with the model. First, the steric signal was removed from the anomalies using the Willis et al. (2004) database. Second, a mean dynamic height from the model was generated from a 16-year forward model run from 1990 through 2006 subject only to NCEP surface forcing and initialized by the North Atlantic ROMS solution (Haidvogel et al. 2000), and it was then added to the SSH anomalies before assimilation to ensure consistency with the model.

Despite both products using identical satellite sources, the RMS difference (RMSD) between the Aviso and CCAR SSH products is relatively large, owing to the problems detailed above. For all aggregate analyses presented here, all model grid points not within the Caribbean Sea (CS) or GOM (every point outside of the Antilles arc) is excluded. The RMSD between the Aviso and CCHAR SSH products in the model region of interest is, on average, ~10 cm. As shown in Fig. 1, there are three areas within the GOM and CS characterized by large differences: the Nicaraguan shelf, the Loop Current (LC), and the Mississippi River outflow. Because both products use the same satellite sources, the main difference is due to the NRT errors during the initial period and the posterior nature of the Aviso product vs the NRT estimate of the CCAR product. The temporal and spatial coverage of the satellites is rather sparse (owing to their nadir-looking nature), and the location of a feature that is not sampled well during a given satellite pass can lead to sampling issues in the CCAR product. The boundary of the LC is an excellent example, and on average, the two products differ in their estimate.

**Fig. 1** The RMSD between Aviso and CCAR SSH in meters. The *top panel* shows a map of RMSD at each model grid point over time, revealing that the two products differ at the extent of the LC, and they exhibit differences near the Mississippi River outflow and on the Nicaraguan shelf. The *bottom panel* shows a time series of the spatially averaged RMSD with an average of ∼ 10 cm over the IAS (ignoring points on the Atlantic side of the Antilles island arc)
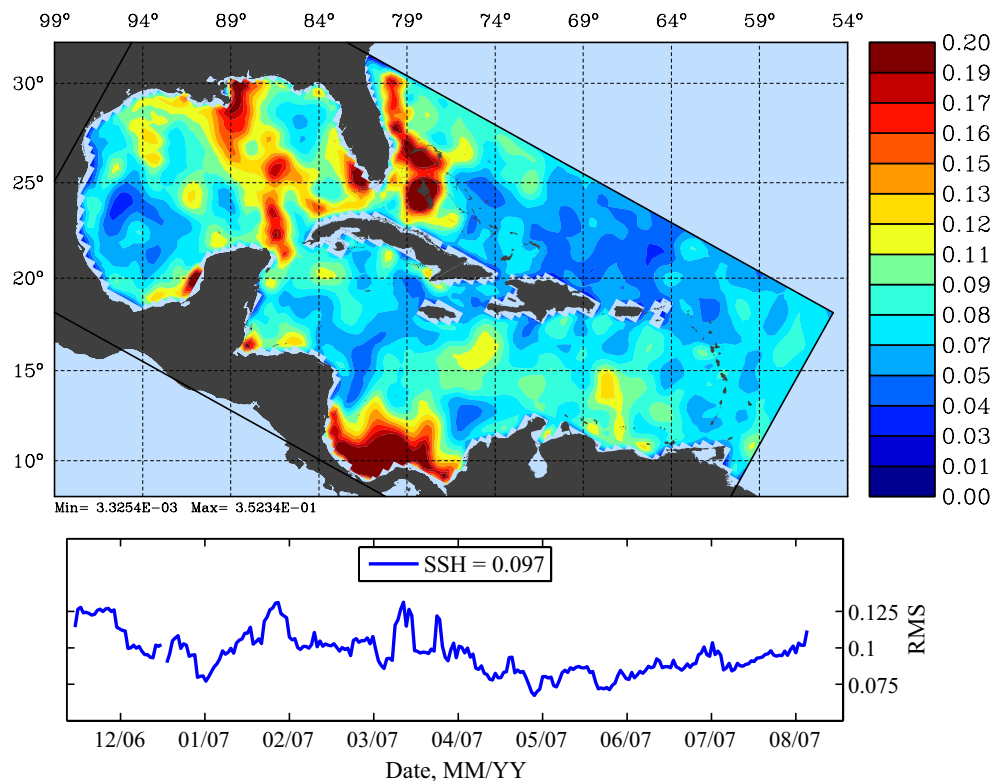


### 3.2 Sea surface temperature data

For SST measurements, the GODAE High-Resolution SST Pilot Program (GHRSST-PP) product (Donlon et al. 2007) was used. The GHRSST-PP L4 is an NRT, 1/20° resolution product available on a daily basis updated with observations made during the previous 24 h. GHRSST-PP combines all available satellite SST measurements (including infrared and microwave) with in situ measurements using a temporal and spatial optimal interpolation scheme (Donlon 2006). The total error for the blended product is lower than the individual errors for each instrument (Reynolds et al. 2002). A minimum error of representativeness of 0.25°C was assigned to **O** in the IS4DVAR application. Like the CCAR SSH, this is a NRT product blended without the benefit of posterior data.

The second SST product is from David Foley of the National Oceanic and Atmospheric Administration, and we will refer to this as the Foley-SST. This blends satellite-based infrared and microwave radiometers to create a 5-day composite, NRT estimate of the bulk layer temperature, inversely weighted by the nominal errors associated with each instrument. For each point at 0.1° spatial resolution, a weighted mean temperature, $T_{ij}$, is calculated from available satellite data (Powell et al. 2008). The Foley-SST product is available in NRT with a 2–3-day lag due to the centered 5-day

composite window. The same 0.25°C minimum error of representativeness is used in the assimilation. Similar to the Aviso processing, this SST product benefits from the use of posterior data.

Figure 2 shows that the major RMSD between the two SST products is associated with the extent of the LC, and there are coastal differences at the Mississippi River outflow and on the Florida shelf. The latter are most likely a combination of using microwave data (which must be used cautiously near land) and the addition of in situ data in the GHRSST product. For the region of interest, there is a mean 0.58°C RMSD with a slight decline during winter months. During summer and early fall, the mixed layer of the IAS shoals to a depth of less than 20 m, providing a nearly homogenous field of SST; however, the RMSD increases during this period.

### 4 Data assimilation results

Different combinations of the observational datasets were assimilated into the ROMS IAS model using the IS4DVAR setup described in Section 2. For simplicity, we will refer to each experiment using the convention listed in Table 1. It should be noted that ExAF uses only delayed, quality-controlled observational data and

**Fig. 2** The RMSD between GHRSST and Foley SST in degrees Celsius. The *top panel* shows a map of pointwise RMSD through time revealing that the two products differ at the extent of the LC and on the Louisiana–Texas shelf. The *bottom panel* shows a time series of the spatially averaged RMSD with an average of ∼ 0.6°C in the IAS
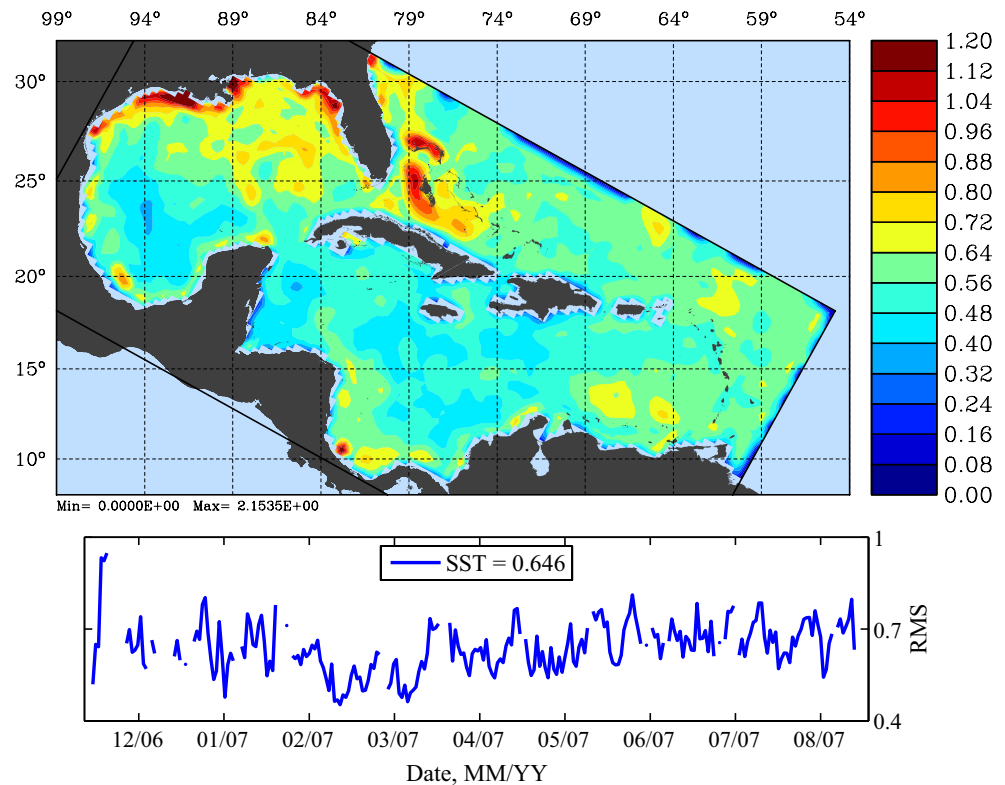


ExCG uses only realtime data. The ExCG experiment was run in NRT onboard the *Explorer of the Seas*. ExAF is the experiment described by Powell et al. (2008). For consistency with ExAF and ExCG, all experiments include any available ADCP data that were sampled on the *Explorer of the Seas*, but these data total less than 1% of all data assimilated, and no ADCP data were available after March 14, 2007, when the ship moved out of the IAS. Powell et al. (2008) found that the addition of the ADCP data had no significant impact on the model estimates of SST or SSH away from the ADCP cruise tracks.

In this section, we will present a summary of the differences between the observations and model assimilation. We will first compare the assimilated model solution and observations by examining the RMSD and the anomaly correlation coefficient (ACC), defined as

$$ACC(x, y) = \sum_{i=1}^{n} (x_i - \bar{x})(y_i - \bar{y})$$

$$\times \left[ \sum_{i=1}^{n} (x_i - \bar{x})^2 \sum_{i=1}^{n} (y_i - \bar{y})^2 \right]^{-\frac{1}{2}}, \quad (8)$$

where $x$ and $y$ are the two scalar fields to be compared, $\bar{x}$ and $\bar{y}$ are their respective mean values, and $n$ is the number of points in space. The RMSD gives us a measure of the difference between $x$ and $y$, and the ACC provides an indication of the agreement between the spatial features of the two fields.

For all experiments, the difference between the model SST and the assimilated observations was similar regardless of the SST or SSH product used, averaging less than 0.6°C RMSD and 0.91 for ACC. In all cases, this is a reduction of more than 50% in RMSD and an increase of 12% in ACC relative to the non-assimilating model. This suggests that, for SST, the nonassimilating model captures the background structure of the flow quite well, but the actual pointwise SST values require some adjustment. These results, and an additional experiment (not shown in Table 1) that did not assimilate SSH, show that SSH data has very little impact on

**Table 1** Overview of assimilation experiments

| Name | Aviso[a] SSH | CCAR SSH | Foley SST | GHRSST-PP[a] SST |
|------|------|------|------|------|
| ExAF | × | | × | |
| ExAG | × | | | × |
| ExCF | | × | × | |
| ExCG | | × | | × |

[a]GODAE products

the assimilation of the SST. In the current setup, only the block diagonal components of **B** are calculated (since $\mathbf{K}_b$ is the identity matrix). Even though SSH and temperature are dynamically related by the model, there are no dynamical constraints relating SSH and temperature explicitly imposed in the cost function. This means that adjustments to the water column affecting the SST can be made independently of the dynamic height. The assimilation reduces the initial SST difference dramatically, and the difference between the assimilated model solution and the observations is similar to the difference between the observation products. There is a level of uncertainty between independent observational products of nearly 0.6°C that is similar to the RMSD of the assimilated model with each set of observations.

As shown in the previous section, the differences between the two observational products can be significant, so particular attention is paid to the RMSD between assimilated model solutions compared to the unassimilated observational product. We compared two experiments in which the same SSH data were assimilated, but the assimilated SST data were different (ExAF compared to ExAG), and compute the RMSD between the model SST and the unassimilated observational product. Figure 3 shows the RMSD map between ExAG and the Foley-SST observations. As anticipated, the

largest differences lie along the margins of the LC and the shallow shelves of the Gulf of Mexico, consistent with Fig. 2. The lower panel of Fig. 3 shows the time series of the RMSD between Foley-SST and ExAG and between Foley-SST and ExAF. When assimilating the GHRSST-PP product, the RMSD relative to the Foley-SST product averages only 0.087°C higher than when assimilating the Foley-SST. Likewise, the ACC between the GHRSST-PP assimilated model solution and the Foley-SST product is identical ($\sim 0.9$) to the case when assimilating the Foley-SST. Although not shown, these comparisons remain unchanged when using the CCAR SSH product, which further suggests that assimilating SSH has little impact on the assimilated temperature structure. The assimilated model solutions of SST compare favorably with both observational products, and the RMSD between the model SST and observations is consistent with the RMSD between the observational products of $O(0.6°C)$.

Varying the SSH products that are assimilated into the model results in significant differences between the model SSH estimates due to the satellite issues discussed earlier. As shown in Section 3, the RMSD between the two observational SSH products is $\sim 10$ cm. The assimilation experiments using the NRT CCAR product (ExCF and ExCG) yield a RMSD between the model SSH and assimilated observations $\sim 7.4$ cm

**Fig. 3** The *top panel* shows the pointwise RMSD through time between ExAG and Foley-SST in degrees Celsius. The *bottom panel* compares the time series of spatial RMSD between ExAF against the Foley-SST, and ExAG and Foley-SST
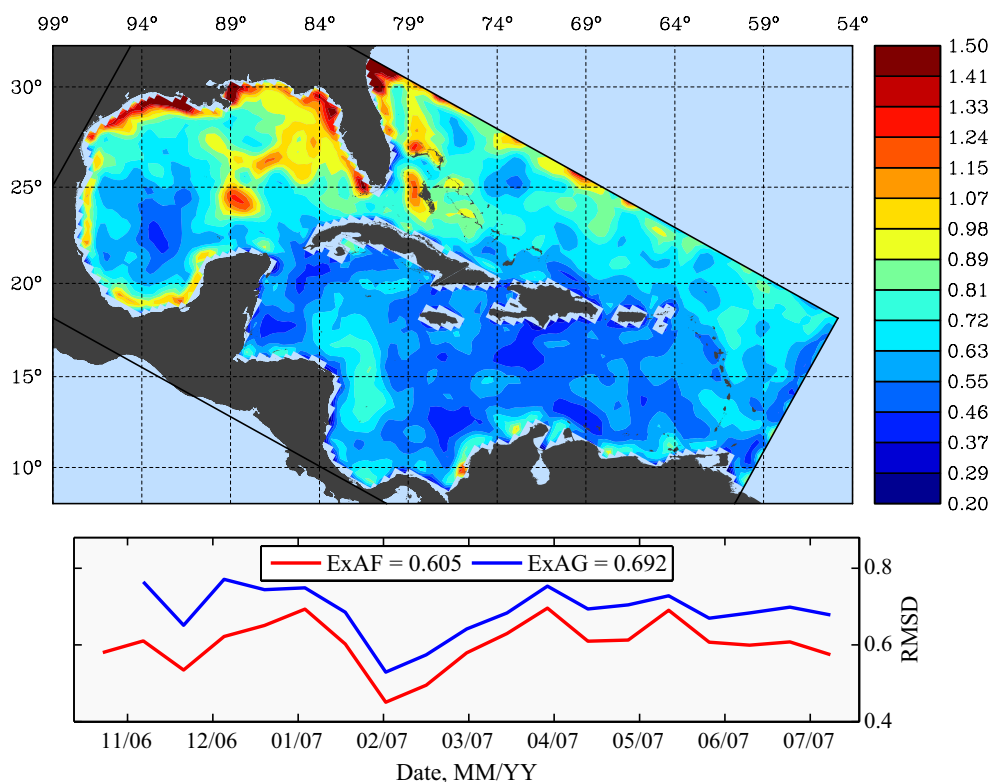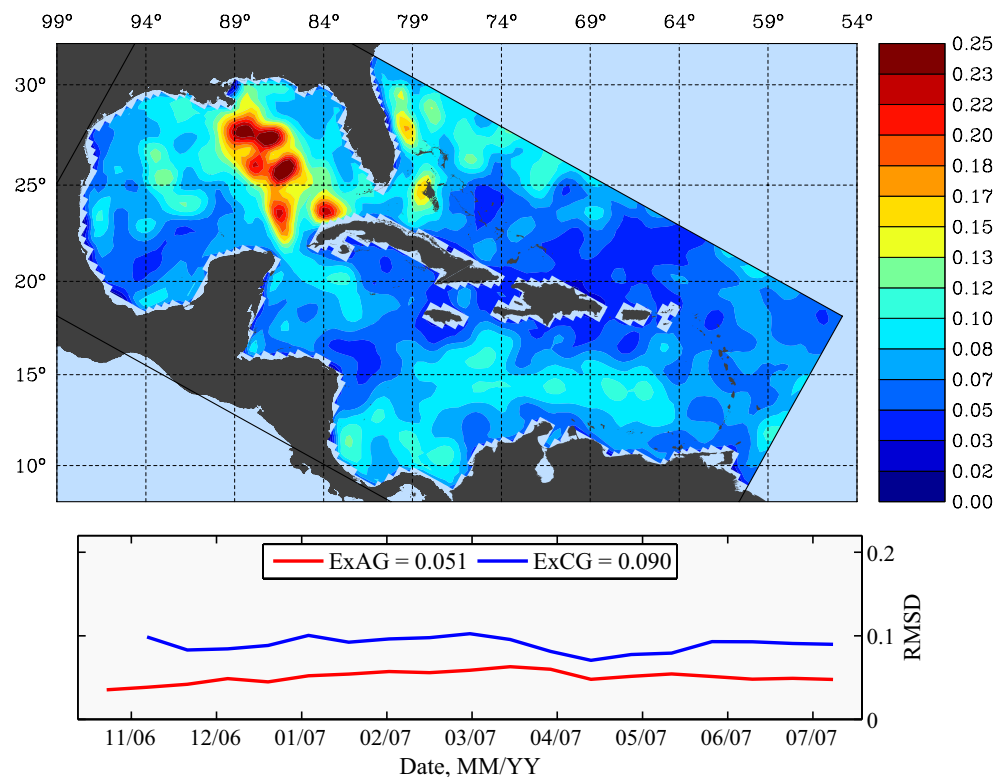
**Fig. 4** The *top panel* shows the RMSD in SSH between ExCG and Aviso SSH in meters. The *lower panel* compares the time series of spatial RMSD of ExAG and ExCG against the Aviso product
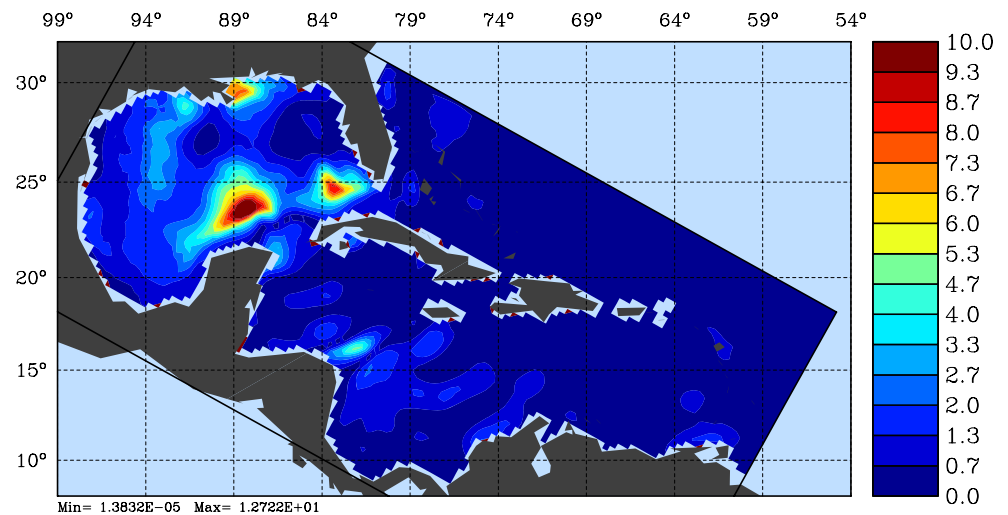


## 5 Analysis error estimates

and $\sim 0.7$ in ACC, an improvement of 50% in RMSD and 96% in ACC compared to the model without data assimilation. For the experiments using Aviso SSH (ExAF and ExAG), the corresponding differences are $\sim 5.2$ cm for RMSD and $\sim 0.85$ for ACC, improvements of 64% and 98%, respectively, as compared to the case when no data are assimilated. The assimilation of the Aviso SSH reduced the RMSD between the model and the CCAR product by 30% compared to the case when no data are assimilated. ExCG possesses larger errors than ExAG on the Nicaraguan shelf; however, the ExCG errors in the vicinity of the LC are less than ExAG. Figure 4 shows the pronounced difference between ExCG and the Aviso observations with $\sim 25$ cm RMSD in the LC and its intrusion into the Gulf of Mexico.

The difference between the SSH from the model assimilation and the observations is similar to the difference between the observation products. The bottom panel of Fig. 4 shows that the model solution obtained by assimilating the CCAR SSH product averages $\sim 9$ cm RMSD compared to the Aviso SSH observations. The ACC falls to $< 0.6$ in the same case. This is due to the satellite issues discussed earlier. In the next section, we will quantitatively determine how the assimilation of each product reduces the prior uncertainties of our ocean state estimates.
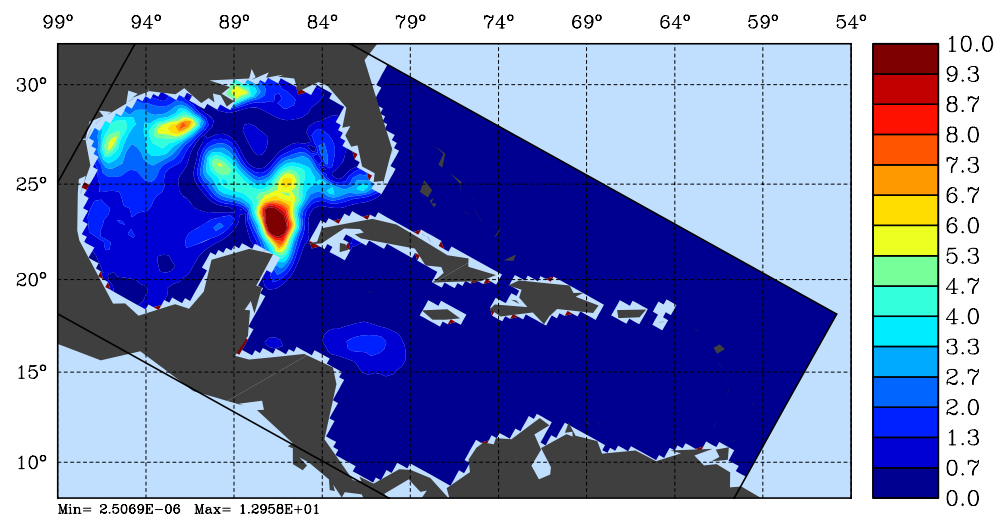
The 4DVAR analysis error, $\mathbf{E}_a$, provides useful information for understanding which regions of prior model uncertainty (as described by $\mathbf{B}$) were reduced through the assimilation of the observational products. The assimilation procedure requires two prior covariance matrices: the background error covariance matrix ($\mathbf{B}$), representing here the variability of the ocean, and the observation error and error of representativeness ($\mathbf{O}$) that, respectively, describe the uncertainty of the observations due to instrument error and the ability of the model in capturing the observed ocean circulation. The analysis error describes the posterior uncertainty of the ocean state estimate given by the final model circulation estimate. By comparing the prior and posterior error estimates for each experiment, we attempt to illustrate and quantify the differences that result from assimilating each observational product. As shown by Gelaro et al. (2002) and Hamill et al. (2002) for the atmosphere, the spatial distribution of prior error reduction is dependent upon observational density. Gelaro et al. (2002) showed significant reductions in regions that had not been previously observed. However, Hamill et al. (2002) showed that the relationship between observational density and analysis error reduction is not obvious, with regions of high observational
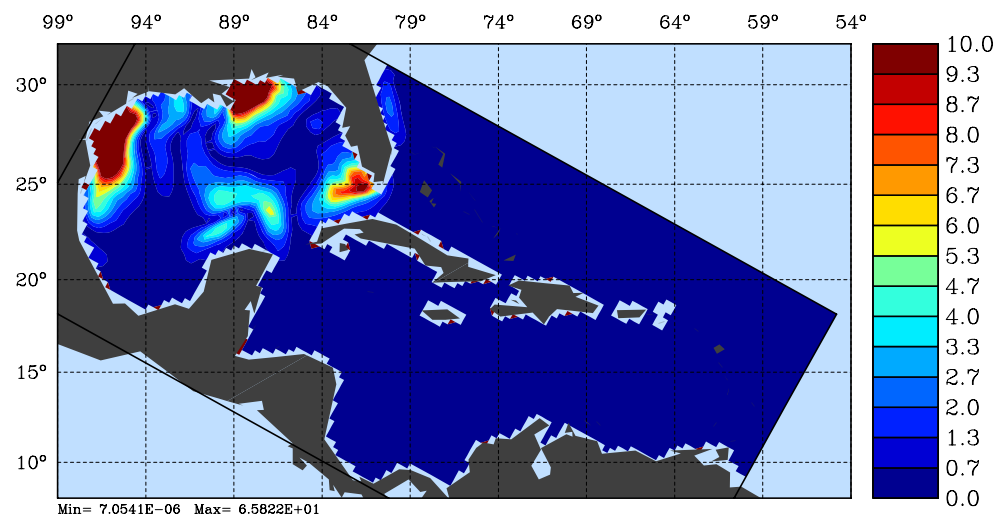
**Fig. 5** The potential temperature component at the mean thermocline depth (50 m) in degrees Celsius of six Hessian eigenvectors from ExAG during a single assimilation period from January 17 through 31, 2007 (**a**–**f**)
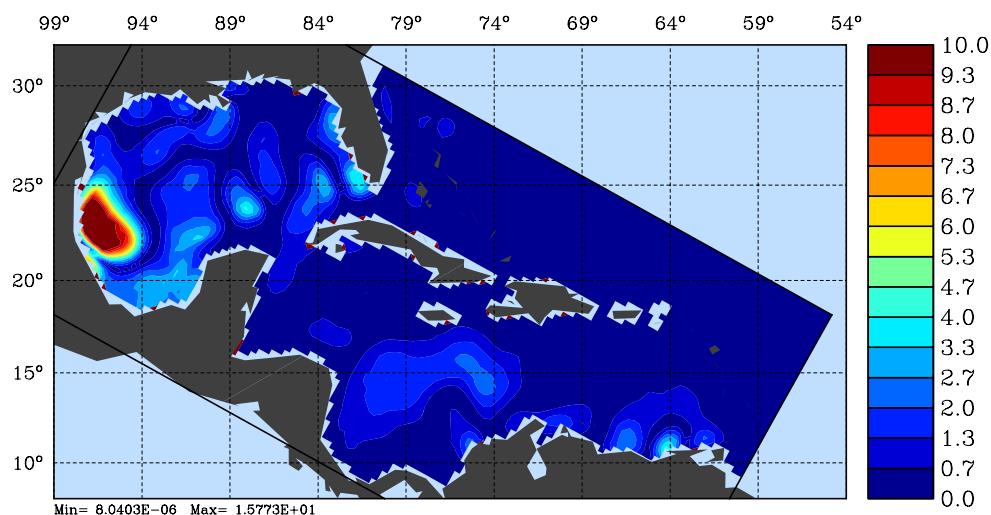


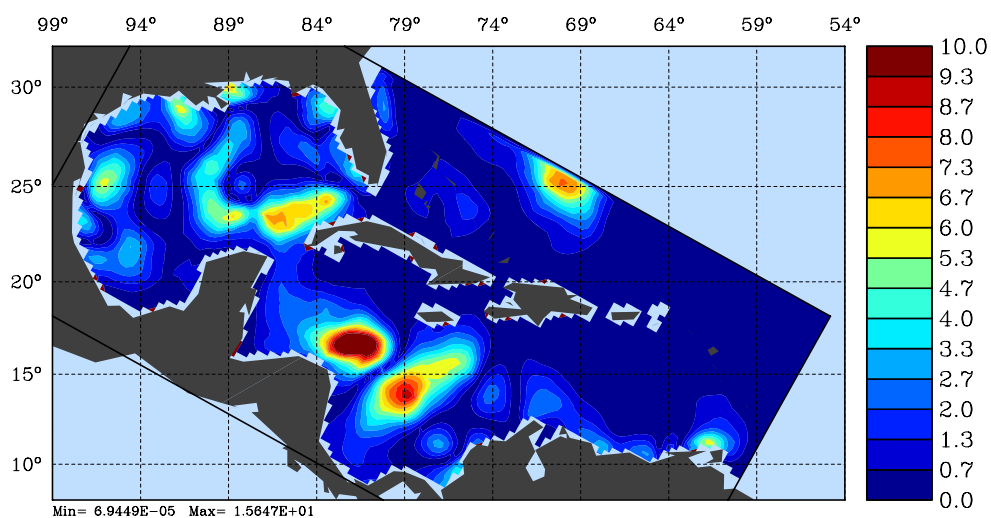(a) $\lambda_1 = 14900$

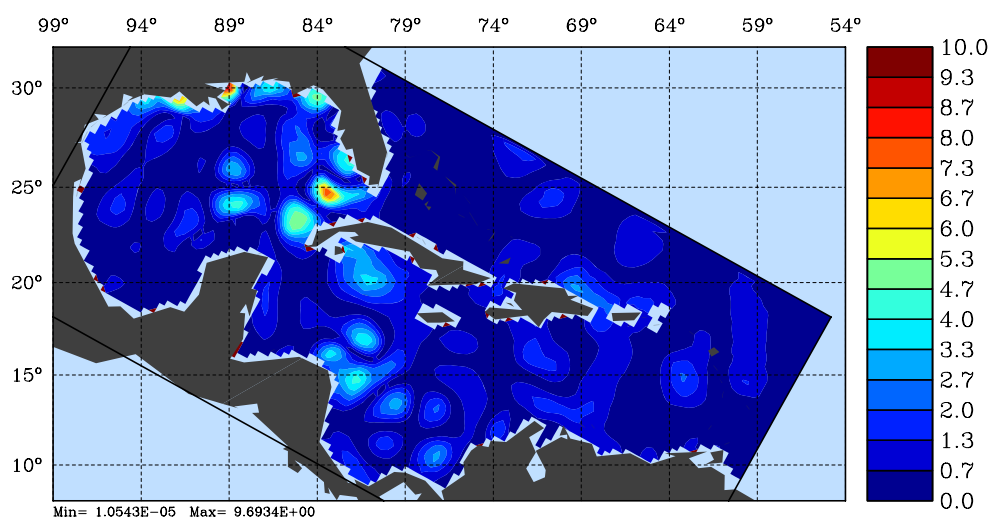(b) $\lambda_6 = 6605$

(c) $\lambda_{13} = 5116$

**Fig. 5** (continued)



Min= 8.0403E−06   Max= 1.5773E+01

(d)  $\lambda_{25} = 3617$



Min= 6.9449E−05   Max= 1.5647E+01

(e)  $\lambda_{45} = 2419$



Min= 1.0543E−05   Max= 9.6934E+00

(f)  $\lambda_{64} = 1069$

density contributing less to the largest inverse Hessian eigenvectors than areas of moderate density. For the experiments shown here, the distribution of observations is generally spatially consistent with surface observations at most ocean grid cells.

Our interest with the analysis error is to compare the analysis error with **B**; however, the analysis error is used in numerical weather prediction to construct the initial forecast errors, and the eigenvectors of the analysis error provide information on the fastest-growing errors (Palmer et al. 1998; Gelaro et al. 2002).

As mentioned earlier, due to computational and storage limitations, we can only generate the estimates of the analysis error variance, represented by the diagonal elements of $\mathbf{E}_a$. Therefore, for the remainder of this discussion, we will concentrate on the diagonal elements of the analysis error. Estimates of the

diagonal of a reduced rank estimate of $\mathbf{E}_a$ were computed from the Hessian eigenvectors according to Eq. 7. For all of the experiments, using 30 inner-loops for the IS4DVAR minimization yielded, on average, $k \approx 15$ Hessian eigenvectors, for which $\epsilon = \|\mathcal{H}_v\mathbf{e}_i^v - \lambda_i\mathbf{e}_i^v\|/\lambda_1 \leq 10^{-4}$.

We chose three separate assimilation periods evenly distributed through the experiment, and increased the number of inner-loop iterations to 100 in order to increase the number, $k$, of eigenvectors with $\epsilon \leq 10^{-4}$ used in Eq. 7 to compare with the standard 30 inner-loop cases. By executing additional inner-loops, the assimilation procedure further improves its estimate of the analysis increment Eq. 3. For each case, the additional inner-loops only reduce the cost function a further 6% on average. The cost function typically decreases very rapidly, and within 20 inner-loops, it



**Fig. 6** The estimated difference in meters between the standard deviations of the background error and the standard deviations of the analysis error for SSH from the GODAE products (ExAG) using 13 and 64 eigenvectors from a single assimilation period of January 17 through 31, 2007 (**a, b**)

(a) $k = 13$

(b) $k = 64$
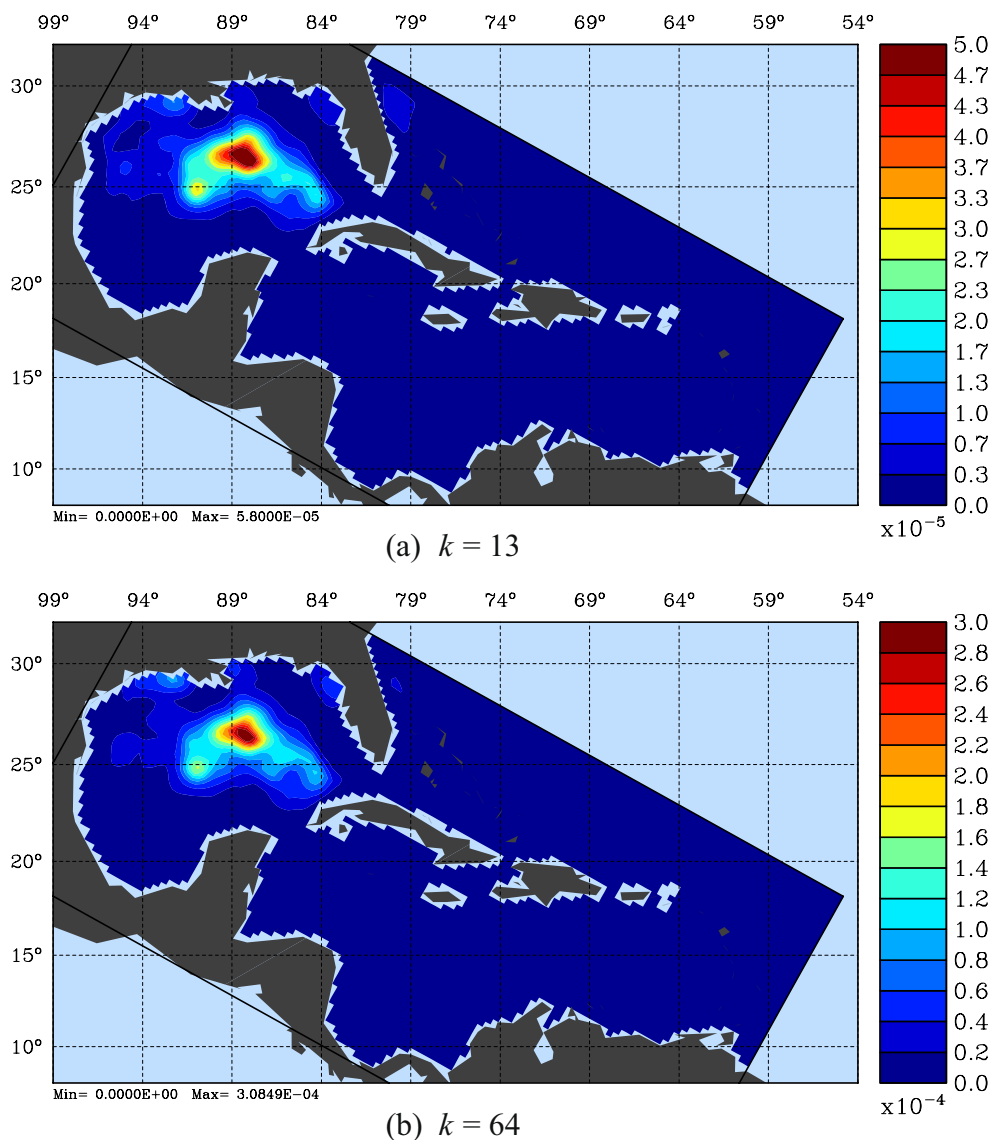
has decreased to ~ 50% of its initial value. With these additional inner-loops, we improve the circulation estimate little, while improving our estimate of $\mathbf{E}_a$. With an improved estimate, we still underestimate $\mathbf{E}_a$ because neither $\mathbf{B}$ nor $\mathbf{O}$ is well-known (Gelaro et al. 2002). To understand what information the additional Hessian eigenvectors provide, we compare eigenvectors from the experiments using 30 and 100 inner-loops.

As an illustrative case, Fig. 5 shows the potential temperature component at the mean thermocline depth from six Hessian eigenvectors for ExAG (GODAE products) from the assimilation of the period January 17 through 31, 2007. The mean thermocline is chosen because it is the region of greatest temperature variance, and it is found to be ~ 50 m during this time period. For this assimilation, 13 (64) converged eigenvectors were identified with $\epsilon \leq 10^{-4}$ during the 30 (100)-inner-loop case. As the eigenvalues decrease,

structures outside of the GOM are revealed; however, these are only described by the eigenvectors not captured during the 30-inner-loop case.

Because the resolution of the model grid and observational products are similar, for most cases, there is a surface observation at each model grid, and during the experiment period, $\mathbf{O}$ has similar spatial structure between the observational products. As shown earlier, $\mathbf{E}_a$ depends on $\mathbf{B}$, $\mathbf{O}$, and the background flow, $\Psi_b(t)$; therefore, due to the similarities in the observational products, $\Psi_b(t)$ will be the primary contributor to the differences between eigenvectors of two different cases. Figure 5 reveals that the maximum amplitude of the Hessian eigenvectors occurs in regions of locally high variance in the background error, particularly in the GOM and LC.

It is evident that, with fewer than 20 Hessian eigenvectors, we may be missing a significant portion of

**Fig. 7** The estimated difference in degrees Celsius between the standard deviations of the background error and the standard deviations of the analysis error for potential temperature at a depth of 50 m from the GODAE products (ExAG) using 13 and 64 eigenvectors from a single assimilation period of January 17 through 31, 2007



(a) $k = 15$



(b) $k = 65$
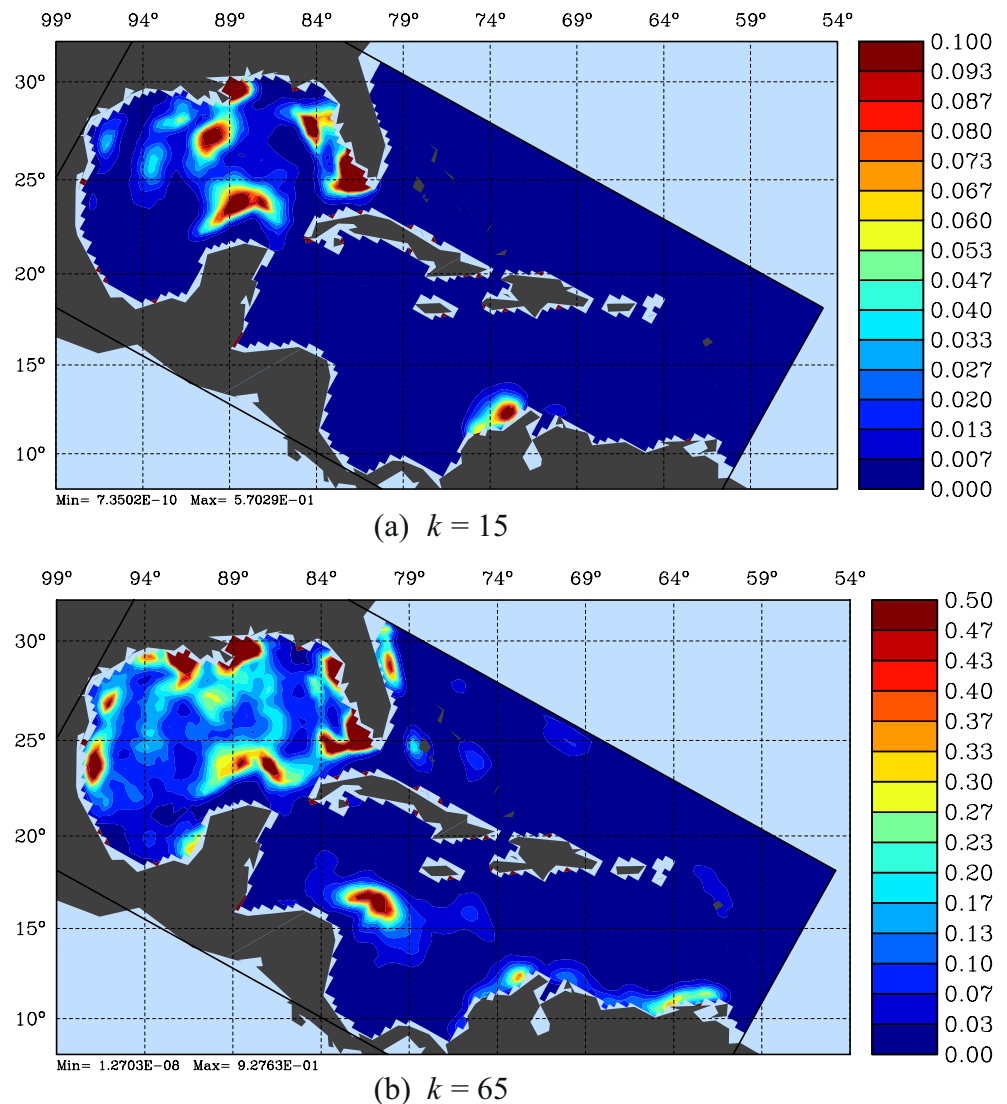
the eigenspectrum. Figure 6 shows the difference between the standard deviations of **B** and estimates of the standard deviations of $\mathbf{E}_a$ for SSH using 13 and 64 Hessian eigenvectors from the same period. While the geographic variations in standard deviation are similar in both cases, increasing the number of eigenvectors increases the magnitude of the differences by only $O(10^{-4})$ m. The difference between **B** and $\mathbf{E}_a$ in SSH is too small to be significant.

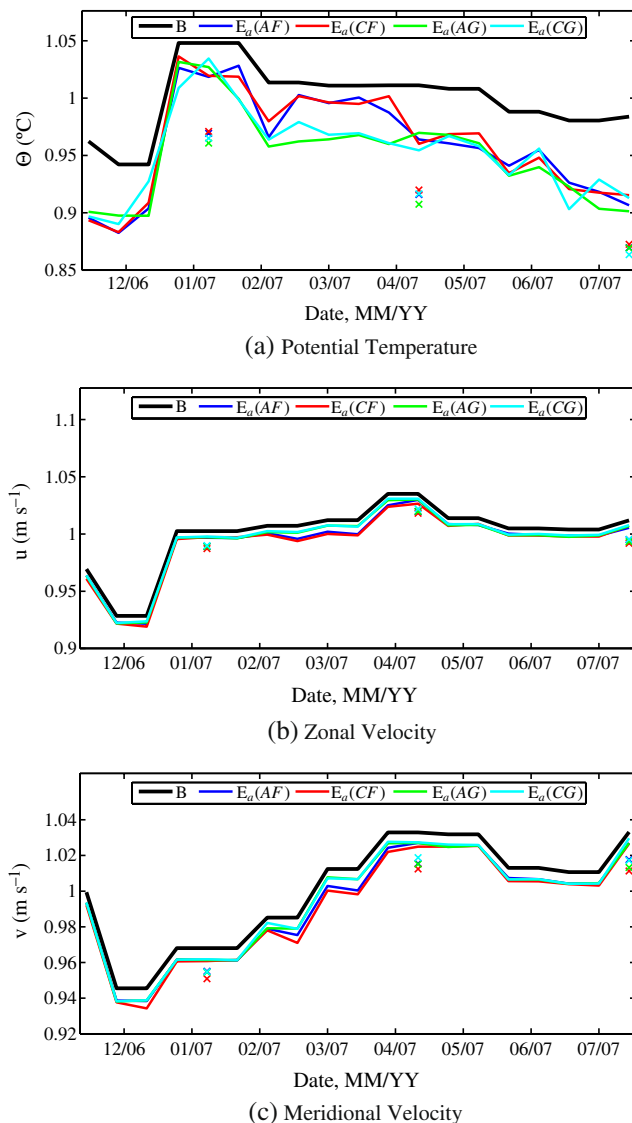As shown in Fig. 5, the eigenvectors identified beyond 30 inner-loops revealed structures outside



**Fig. 9** The difference between estimates of the diagonal $\mathbf{E}_a$ for potential temperature in degrees Celsius from ExAG and ExAF along a transect through the Gulf of Mexico from Mississippi to Cuba from the February 28–March 14, 2007, assimilation period. The $\mathbf{E}_a$ estimate from the GHRSST-PP product improves our estimate of **B** over 0.25°C in the Mississippi River outflow from the Foley-SST product



(a) Potential Temperature



(b) Zonal Velocity



(c) Meridional Velocity

**Fig. 8** Time series comparing $[\text{trace}(\mathbf{B})]^{\frac{1}{2}}$ with $[\text{trace}(\mathbf{E}_a)]^{\frac{1}{2}}$, normalized by the annual mean from $[\text{trace}(\mathbf{B})]^{\frac{1}{2}}$ for each 30-inner-loop ($\sim 15$ eigenvectors) assimilation for three different fields, potential temperature, zonal, and meridional velocities. The results of the three 100-inner-loop ($\sim 62$ eigenvectors) experiments are shown by *crosses* (**a–c**)
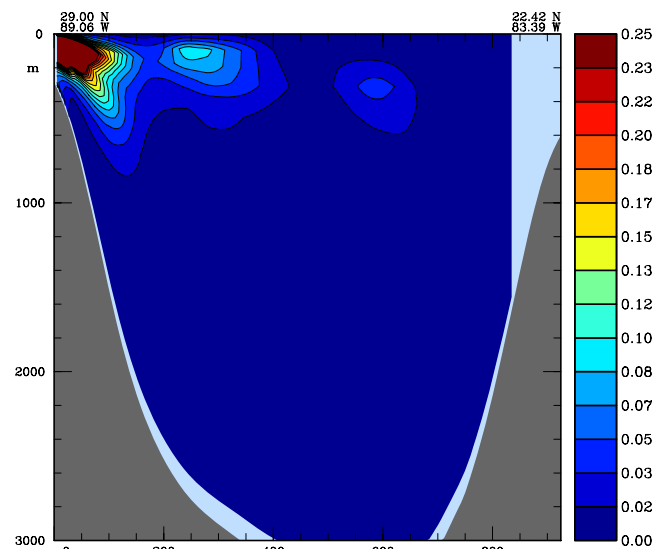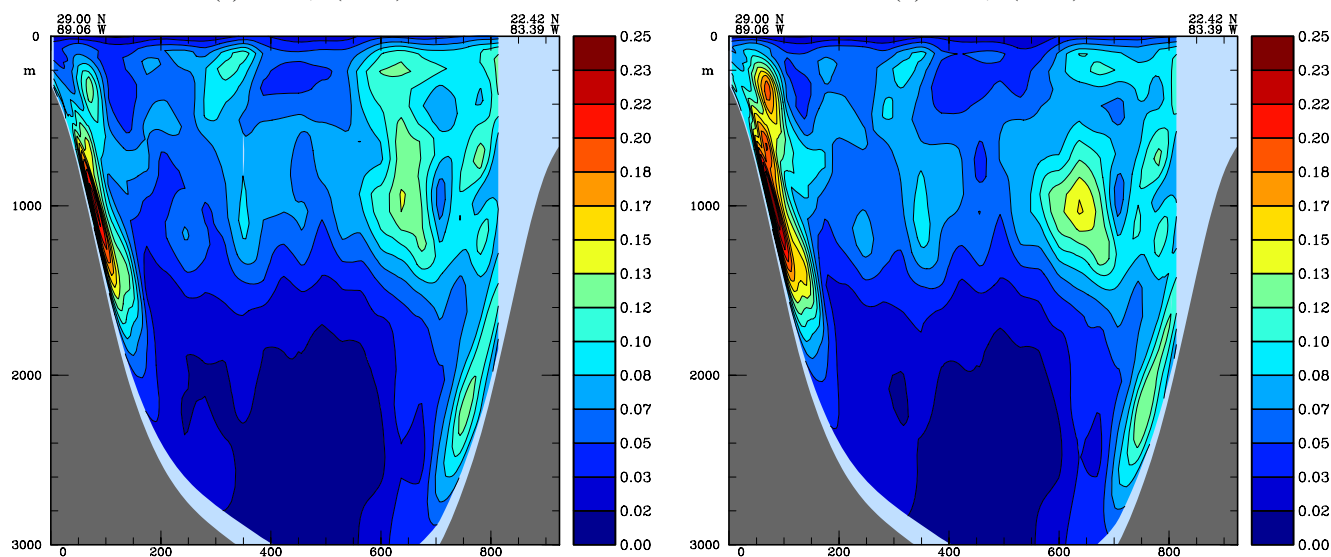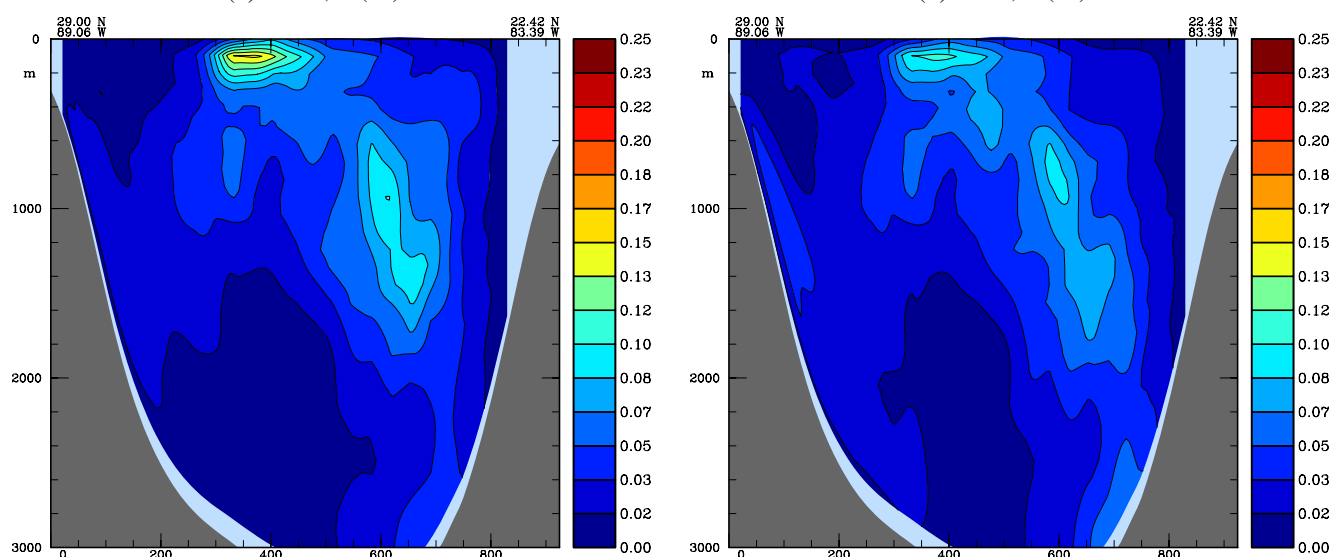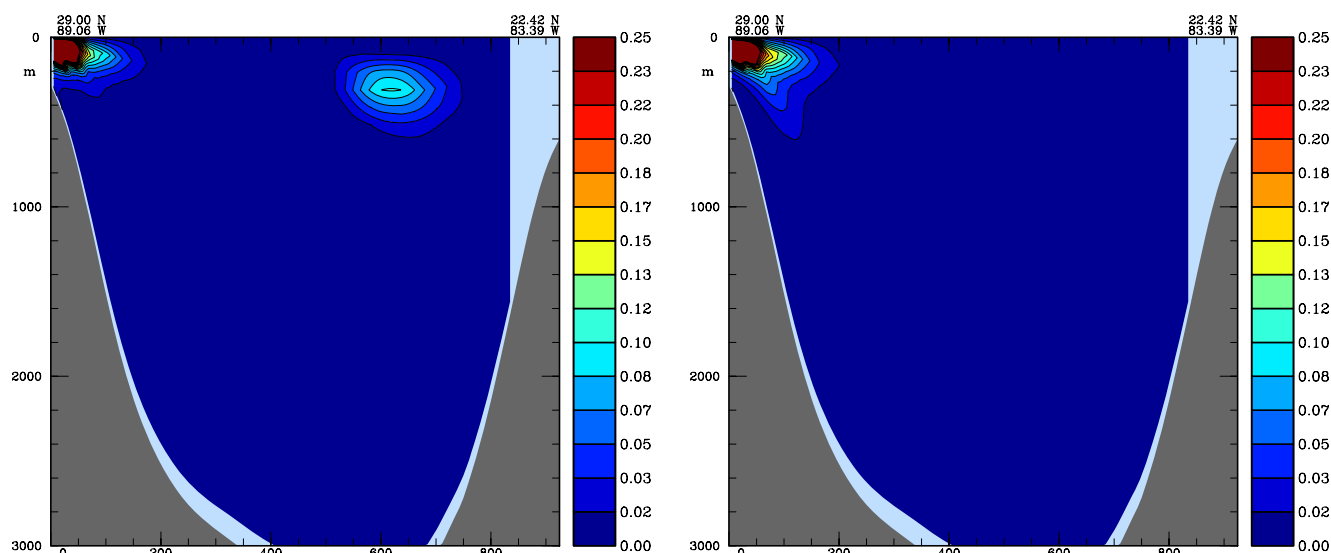
of the GOM. The impact on $\mathbf{E}_a$ of increasing the number of Hessian eigenvectors on the standard deviation of errors in 50-m potential temperature is more significant, as shown in Fig. 7, which shows the difference between the standard deviations of **B** and $\mathbf{E}_a$. Despite the difference in magnitude, the spatial structures of the two estimates have similar structures with significant peaks on the Campeche Bank (north of Yucatan), Western Florida Shelf, and South of Mississippi. According to the SST, the LC had intruded deep into the GOM, with a maximum extent beyond 26°30'N, and (as shown in the SSH) a cyclonic eddy was preventing further intrusion. The cyclonic eddy has a signature in the difference plots south of Mississippi, as this feature is present in the model and observations, helping to reduce the prior potential temperature uncertainty in the region of high eddy activity. The Campeche Bank is the boundary to the west of the LC. When the LC is intruded, there is strong positive potential vorticity at the northern extent of the bank, as it acts to mirror the vorticity of the LC (Chérubin et al. 2006). It appears that, by properly resolving the LC location, there is a reduction of the

**Fig. 10** Difference between the standard deviations of background error and estimated analysis error for ExAG (GODAE data) and ExCF (non-GODAE data) without ADCP data assimilated. Transects across the GOM for three fields are shown: potential temperature, zonal, and meridional velocities (**a–f**)

(a) ExAG, Θ (°C)

(b) ExCF, Θ (°C)

(c) ExAG, $u$(m s$^{-1}$)

(d) ExCF, $u$(m s$^{-1}$)

(e) ExAG, $\upsilon$(m s$^{-1}$)

(f) ExCF, $\upsilon$(m s$^{-1}$)

uncertainties around the northern edge of the Campeche Bank. Towards the Florida Channel, the LC is bounded by the Florida shelf, and it directly influences processes on the shelf. Similarly, in this region of activity, there is a marked decrease in the prior uncertainty during this time.

The eigenvector corresponding to $\lambda_2 5$ contributes to the main difference in the Western GOM and the eigenvector corresponding to $\lambda_4 5$ to the CS. These are the two major differences between the estimates, with the remaining patterns covering a similar area with collocated peaks of differing magnitude. Equation 6 suggests that only eigenvectors with eigenvalues sufficiently different from 1 will cause the Hessian in *v-space* to differ significantly from the identity matrix, and in Fig. 5, we see that the eigenvalues are sufficiently large. As noted by Fisher and Courtier (1995), the similar error structures that result from differing numbers of Hessian eigenvectors may mean that the reduced rank estimates of $\mathbf{E}_a$ can be appropriately rescaled to account for the remaining unknown eigenvectors. These pattern similarities suggest that estimates generated by the assimilation procedure with relatively few Hessian eigenvectors will provide useful information.

To understand the reduction of $\mathbf{B}$ as described by estimates of $\mathbf{E}_a$ in toto, the square roots of trace($\mathbf{B}$) and trace($\mathbf{E}_a$) were calculated for each assimilation period. Figure 8 show the trace estimates of the seasonally varying $\mathbf{B}$ and from each estimate of $\mathbf{E}_a$ for potential temperature and velocity using the 30-inner-loop cases (which average $k \approx 15$ eigenvectors), each normalized by the annual mean of the $\mathbf{B}$ trace estimates. Additionally, the results of each of the three 100-inner-loop experiments are shown (averaging $k \approx 62$ eigenvectors). SSH is not included because, as shown in Fig. 6, the posterior error estimates are very similar to the prior errors.

For all experiments, the difference between trace($\mathbf{B}$) and trace($\mathbf{E}_a$) is greatest for potential temperature. Both SSH products lead to a similar reduction (and are unaffected by the choice of the SSH product), except during the period from February through April, when the number of available Foley-SST data fell by 30% with sparsely distributed values around the domain. As shown in Fig. 7, virtually all of the reduction in the error estimate occurs in the GOM. To understand how the missing data impact the diagonal estimates of $\mathbf{E}_a$, the difference between potential temperature components of the diagonal of $\mathbf{E}_a$ from ExAG and ExAF are shown along a transect in the GOM in Fig. 9. The loss of observations had the biggest effect in the vicinity of the Mississippi River outflow, which results in a large prior uncertainty, $\mathbf{B}$. Furthermore, during this period,

there is a dramatic cooling of the waters, as shown in climatology of local buoys. The loss of observations during a time of higher variance is apparent in the estimates of the diagonal of $\mathbf{E}_a$ from ExAF and ExCF.

Figure 8b, c shows that, although we are primarily assimilating surface data (with very sparse ADCP data during the first half of the experiment), there is a small reduction in our estimate of the prior error in velocity as well. Interestingly, during the period of degraded observations from Foley-SST, there is an improvement in velocity for the products that use it. With fewer data, there is a greater degree of freedom to perturb the velocity and SSH fields, which may account for the slight reduction in velocity uncertainty during the period with fewer observations. Regardless of the period, there is an overall reduction of the uncertainty in the total velocity.

To understand where the reductions in $\mathbf{E}_a$ compared to $\mathbf{B}$ are occurring, we compare transects across the GOM from ExAG and ExCF for the assimilation period of August 1 through 15, with no available ADCP data to assimilate. Figure 10 shows the estimated difference between standard deviations of $\mathbf{B}$ and standard deviations computed from the diagonal of $\mathbf{E}_a$ for potential temperature, zonal, and meridional velocities. The temperature structure shows that the Mississippi River outflow (which has the largest variance in the prior) is the region of greatest reduction in both products, but in the GODAE case, there is additional improvement in the core of the LC. While only assimilating surface data, we see in Fig. 10 significant uncertainty reduction in both velocity components. Although the magnitudes vary, the structure of $\mathbf{E}_a$ is similar for each experiment, which suggests that the dynamics required to perturb each flow were similar across experiments.

## 6 Conclusions

One objective of the GODAE program is to provide data products suitable for use in ocean data assimilation, and we compare two of these products with other similarly processed data. Using IS4DVAR, these data were assimilated into an ocean model of the IAS to compare their impacts on estimates of the ocean circulation. In each case, the RMSD between the assimilated model and the observations was less than or equal to the RMSD between the two observational products themselves. This is an important consideration because data assimilation would not be expected to generate a state estimate that is less than the uncertainty between two independently produced data products. The reliance of NRT data in the CCAR-SSH product creates

a significant issue during both times of degraded satellite performance and periods of sparse sampling. This suggests that higher observational errors should be prescribed in **O** for NRT products.

Utilizing the iterative procedure of the IS4DVAR method, we were able to compute eigenvectors of the Hessian matrix, which allowed us to estimate the analysis error covariance matrix, $\mathbf{E}_a$. This covariance estimate gives us a posterior uncertainty of the model circulation and requires very little processing in addition to the assimilation procedure. The spatial structures of the diagonal of $\mathbf{E}_a$ created with fewer Hessian eigenvectors were consistent with experiments using greater numbers of eigenvectors; however, significant portions of the differences between **B** and $\mathbf{E}_a$ remain unexplained with fewer eigenvectors. This result is similar to Fisher and Courtier (1995) for the atmosphere, where it is suggested that the converged eigenvalues could be scaled to account for the unsolved portion of the eigenspectrum and Gelaro et al. (2002) where, in linear regimes, fewer vectors are required. In all cases, the reduction of the analysis error was greatest where the background error covariance was largest. This suggests that, as the assimilation proceeds, **B** should be adjusted to account for the explained variance that has been obtained during the assimilation. This is consistent with the findings of Powell et al. (2008). Although the magnitude of the $\mathbf{E}_a$ is uncertain (due to using a low-rank estimate) and may require rescaling due to the limited number of Hessian eigenvectors used, the robust spatial patterns of analysis error that emerge from using different numbers of eigenvectors suggest that we may be able to quantify errors in the geographic location of important circulation features, such as eddies, that are present in the analysis.

The various observational products were found to reduce the background error to a similar degree, but in the instances where more Hessian eigenvectors were employed, the analysis error indicated that the GODAE products reduced the uncertainty in the LC (both in potential temperature and velocity) more than the non-GODAE products. Despite assimilating only surface data (ADCP was used sparingly during the initial months), we find significant reductions in the background uncertainty in the baroclinic structure and velocity field after the assimilation. This is a further illustration of the advantage in using 4DVAR methods that utilize the model physics to adjust the initial state.

## References

Chérubin LM, Morel Y, Chassignet EP (2006) Loop current ring shedding: the formation of cyclones and the effect of topography. J Phys Oceanogr 36:569–591

Courtier P, Thépaut JN, Hollingsworth A (1994) A strategy for operational implementation of 4D-Var, using an incremental approach. Q J R Meteorol Soc 120:1367–1387

Derber J, Rosati A (1989) A global oceanic data assimilation system. J Phys Oceanogr 19:1333–1347

Donlon C, Robinson I, Casey KS, Vazquez-Cuervo J, Armstrong E, Arino O, Gentemann C, May D, LeBorgne P, Piollé J, Barton I, Beggs H, Poulter DJS, Merchant CJ, Bingham A, Heinz S, Harris A, Wick G, Emery B, Minnett P, Evans R, Llewellyn-Jones D, Mutlow C, Reynolds RW, Kawamura H, Rayner N (2007) The global ocean data assimilation experiment high resolution sea surface temperature pilot project. Bull Am Meteorol Soc 88(8):1197–1213

Donlon CJ (2006) The Global Ocean Data Assimilation Experiment High Resolution Sea Surface Temperature Pilot Project (GHRSST-PP) data processing specification version 1.7 (GDSv1.7). Technical report, GODAE Project Office, UK Met Office

Draper NR, Smith H (1966) Applied regression analysis. Wiley, New York

Fairall CW, Bradley EF, Rogers DP, Edson JB, Young GS (1996) Bulk parameterization of air-sea fluxes for tropical ocean–global atmosper coupled-ocean atmosphere response experiment. J Geophys Res 101:3747–3764

Fisher M (1998) Minimization algorithms for variational data assimilation. In: Seminar on recent developments in numerical methods for atmospheric modelling, ECMWF, Reading, 7–11 September 1998

Fisher M, Courtier P (1995) Estimating the covariance matrices of analysis and forecast error in variational data assimilation. Technical Report 220, European Centre for Medium-Range Weather Forecasts

Gejadze Y, Le Dimet F-X, Shutyaev V (2008) On analysis error covariances in variational data assimilation. SIAM J Sci Comput 30:1847–1874

Gelaro R, Rosmond T, Daley R (2002) Singular vector calculations with an analysis error variance metric. Mon Weather Rev 130:1166–1186

Golub GH, Van Loan CF (1989) Matrix computations. Johns Hopkins University Press, Baltimore

Haidvogel DB, Arango HG, Hedstrom K, Beckmann A, Malanotte-Rizzoli P, Shchepetkin AF (2000) Model evaluation experiments in the North Atlantic Basin: simulations in nonlinear terrain-following coordinates. Dyn Atmos Ocean 32:239–281

Hamill TM, Snyder C, Morss RE (2002) Analysis-error statistics of a quasigeostrophic model using three-dimensional variational assimilation. Mon Weather Rev 130:2777–2790

Kistler R, Kalnay E, Collins W, Saha S, White G, Woolen J, Chelliah M, Ebisuzaki W, Kanamitsu M, Kousky V,

van den Dool H, Jenne R, Fiorino M (2001) The NCEP/NCAR 50-year reanalysis. Bull Am Meteorol Soc 82:247–268

Le Traon PY, Ducet N, Dibarboure G (2001) Use of a high resolution model to analyze the mapping capabilities of multiple-altimeter missions. J Atmos Ocean Tech 18:1277–1288

Leben RR, Born GH, Engebreth BR (2002) Operational altimeter data processing for mesoscale monitoring. Marine Geod 25:3–18

Levitus S, Burgett R, Boyer T (1994) World ocean atlas 1994 volume 4: temperature. In: NOAA Atlas NESDIS 4, page 132 pp. U.S. Department of Commerce, Washington, DC

Marchesiello P, McWilliams JC, Shchepetkin A (2001) Open boundary conditions for long-term integration of regional oceanic models. Ocean Model 3:1–20

Palmer TN, Gelaro R, Barkmeijer J, Buizza R (1998) Singular vectors, metrics, and adaptive observations. J Atmos Sci 55:633–653

Parrish DF, Derber JC (1992) The national meteorological center's spectral statistical-interpolation analysis system. Mon Weather Rev 120:1747–1763

Pascual A, Pujol M-I, Larnicol G, Le Traon P-Y, Rio M-H (2007) Mesoscale mapping capabilities of multisatellite altimeter missions: first results with real data in the Mediterranean Sea. J Marine Syst 65:190–211

Powell BS, Arango HG, Moore AM, Di Lorenzo E, Milliff RF, Foley D (2008) 4DVAR data assimilation in the Intra-Americas Sea with the Regional Ocean Modeling System (ROMS). Ocean Model 25:173–188

Reynolds RW, Rayner NA, Smith TM, Stokes DC, Wang W (2002) An improved in situ and satellite SST analysis for climate. J Climate 15:1609–1625. doi:10.1175/1520-0442(2002)015<1609:AIISAS>2.0.CO;2

Shchepetkin AF, McWilliams JC (2005) The regional oceanic modeling system: a split-explicit, free-surface, topography-following-coordinate ocean model. Ocean Model 9:347–404

Tshimanga J, Gratton S, Weaver AT, Sartenaer A (2008) Limited-memory preconditioners with application to incremental four-dimensional variational data assimilation. Q J R Meteorol Soc 134:751–769

Warner JC, Sherwood CR, Arango HG, Signell RP (2005) Performence of four turbulence closure models implemented using a generic length scale method. Ocean Model 8:81–113

Weaver A, Courtier P (2001) Correlation modelling on the sphere using generalized diffusion equation. Q J R Meteorol Soc 127:1815–1846

Willis JK, Roemmich D, Cornuelle B (2004) Interannual variability in upper ocean heat content, temperature, and thermosteric expansion on global scales. J Geophys Res 109. doi:10.1029/2003JC002260c